Automatic Containment of Field Exposure for Roadway Wireless Electric Vehicle Charger

Yang Yang, Jingyu Wang, *Student Member, IEEE*, Zhicong Huang, *Member, IEEE*, Io-Wa Iam, *Student Member, IEEE*, and Chi-Seng Lam, *Senior Member, IEEE*

***Abstract*— Inductive power transfer (IPT) has found application prospect in dynamic wireless electric vehicle (EV) charging as it can avoid the constraints of physical connection. With the commonly used LCC compensation, the ground-assembled transmitter coil is always excited by a fixed standby current even if there is no receiver coil coverage. As for dynamic wireless PT (DWPT) systems, even without EV charging, the underground transmitter coils typically remain activated at full power output to wait for the receivers in most cases, resulting in huge standby current and magnetic exposure safety concerns. In this article, we proposed a method for automatic containment of field exposure caused by standby current in the transmitter coil of wireless chargers, which applies LCC compensation networks requiring only primary-side control with the elimination of wireless feedback communication and extra detection. The wireless chargers can be automatically deactivated once EVs depart, as well as automatically activated once detecting the presence of EVs. Also, its excellent interoperability for different loads and types of compensation topology has been well analyzed and then verified. Moreover, experiments demonstrate that the magnetic field exposure is merely 11.66% of the ICNIRP 2010 standard exposure limit with the proposed modulation, which is suppressed by 94.64% than before.**

***Index Terms*— Automatic activation, automatic deactivation, dynamic wireless power transfer (DWPT), field exposure, interoperability.**

I. Introduction

With the increasing pressure on global fossil fuel consumption and environmental pollution in recent years, electric vehicles (EVs) are more attractive than ever as they are powered by a cleaner source of energy, electricity [1]. However, due to the exposed plugs and damaged cables, conventional plug-in charging methods can easily cause safety accidents [2]. Aiming to eliminate the drawbacks of physical contact, the inductive power transfer (IPT) technique has been adopted for EV charging that transfers power via magnetic coupling between the transmitter side and the receiver side [3], [4], [5], [6]. More importantly, it provides a prospective solution of dynamic wireless PT (DWPT) system, which can charge the moving EVs on the road [7], [8], [9].

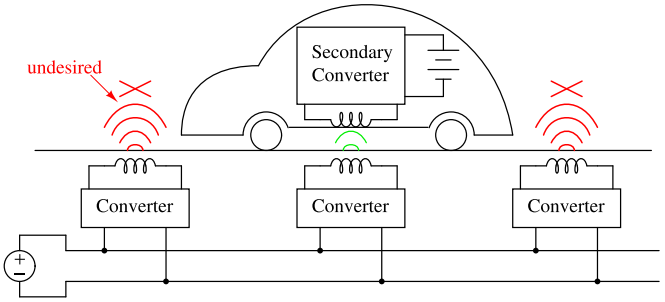

Fig. 1. Magnetic exposure caused by the standby current in the DWPT system.

As for a typical DWPT system, its transmitter coils as chargers are fully deployed underground to deliver power for the moving EVs through magnetic coupling [10], [11]. Yet, each underground charger generally maintains full power output even in the standby state (no EV is being charged). However, the lack of the operations of deactivation and activation for chargers would result in a high standby current in the transmitter coils, which causes a waste of power and even the undesired magnetic exposure to the surrounding area as shown in Fig. 1.

To reduce the undesired magnetic exposure, it is an intuitive idea to apply active electromagnetic exposure shielding solutions using the opposite magnetic fields produced by the conductor current loop, as demonstrated in [12] and [13]. Alternatively, some passive shielding solutions can be adopted, such as [14] using ferromagnetic materials and coils to channel the leakage flux, [15] designing a reactive resonant current loop to cancel the magnetic field, and [16] using an auxiliary coil between the transmitter and receiver coils to reduce the electromagnetic interference at the specific *n*th harmonic frequency. Likewise, [17] and [18] use a double-shield coil with a four-capacitor phase shifter which generates a canceling

Manuscript received 1 September 2022; revised 26 November 2022; accepted 6 January 2023. Date of publication 13 January 2023; date of current version 13 September 2023. This work was supported in part by the National Natural Science Foundation of China under Grant 52007067; in part by the Natural Science Foundation of Guangdong Province under Grant 2022A1515011581; and in part by the Science and Technology Development Fund of Macao Special Administrative Region (FDCT) under Grant 0028/2020/A1, Grant 0014/2021/ITP, Grant SKL-AMSV(UM)-2020-2022, and Grant SKL-AMSV(UM)-2023-2025. *(Corresponding author: Zhicong Huang.)*

Yang Yang, Jingyu Wang, and Zhicong Huang are with the Shien-Ming Wu School of Intelligent Engineering, South China University of Technology, Guangzhou 510006, China (e-mail: zhiconghuang@scut.edu.cn).

Io-Wa Iam is with the State Key Laboratory of Analog and Mixed-Signal VLSI, the Institute of Microelectronics, and the Department of Electrical and Computer Engineering, Faculty of Science and Technology, University of Macau, Macao 999078, China, and also with Smarmac Technology Company Ltd., Macao 999078, China (e-mail: yc07461@um.edu.mo).

Chi-Seng Lam is with the State Key Laboratory of Analog and Mixed-Signal VLSI, the Institute of Microelectronics, and the Department of Electrical and Computer Engineering, Faculty of Science and Technology, University of Macau, Macao 999078, China (e-mail: cslam@um.edu.mo).

Digital Object Identifier 10.1109/TTE.2023.3236684

magnetic field to reduce the leakage magnetic field. The additional cost of exposure cancellation is inevitable, and also, it is not practical for the DWPT system because the shielding solutions merely suppressed undesired magnetic exposure rather than reduced its generation essentially. Although these passive designs can reduce the magnetic field exposure of the transmitter coils to some extent, they cannot dynamically reduce the standby current according to whether the transmitter is covered by a receiver or not. To be more specific, if there is no receiver, the transmitter with shielding still emits a large magnetic field.

The active EVs' detection techniques are available to assist in the containment of the field exposure for the DWPT system, in which essentially the DWPT system achieves deactivation and activation of the chargers by control of power delivery after judging the position of EVs. In some studies, [19] and [20], multiple auxiliary coils are used to detect the positions of EVs. Similarly, a solution proposed in [21] uses additional filters to detect the location of the EV pad. Alternatively, extra tunneling magnetoresistance (TMR) sensor can be adapted to sense the magnetic field generated by the detection coil wrapped around the outside of the receiver coil underneath EV [22], but the detection coil may cause cross-coupling interference. The above solutions require adding extra coils or sensors resulting in high expenses. However, with the elimination of extra components, a dual-loop controller is proposed in [23] to activate the segmented primary coils. Nevertheless, it increases the complexity of system design.

On the other hand, it is a straightforward way to use wireless communication for activation and deactivation with the operation of the transmitter relying on the wireless feedback signal transmitted from the EV. However, the wireless feedback signal may be affected by the strong electromagnetic field, and the transmission error may be harmful to the reliability of the control, which makes the DWPT system less rugged. Therefore, some studies have been carried out to eliminate wireless feedback, such as [24], [25], and [26]. Hence, in practice, it is challenging to obtain a simple and effective EV detection approach for the deactivation and activation of the chargers without auxiliary circuits.

In addition, interoperability is also significant for EVs' detection approach in practice, but unfortunately, in previous works, it has not been fully considered. The above-mentioned position-sensorless algorithm in [27] is only applicable for the specific parallel compensation receiver circuit accompanying a boost converter, which is not interoperable for EV detection. It is reported in [28] that a multiple transmitter DWPT system makes use of the reflected reactance from the receiver to automatically adjust the field strength of the coupling section. Although not limited to applying for a specific receiver circuit, it requires the turns ratio of the magnetic coupler within a certain range to reduce the reactive component, which limits the design of system parameters resulting in low interoperability. To further improve the interoperability, a detection scheme uses free resonant currents of the transmitter coil to detect small coupling variations between neighboring coils while EVs move over them [29], [30], which is suitable for all the magnetic pad topologies. However, it requires a short distance between the underground chargers to continuously detect the arrival of EVs, which increases the consumption of coils laid under the road. Comparisons with the state-of-the-art works have been added, as given by Table I. It can be observed that almost all these studies require extra shielding or sensors. And none of these studies considered suppression of current or magnetic field and the interoperability at the same time.

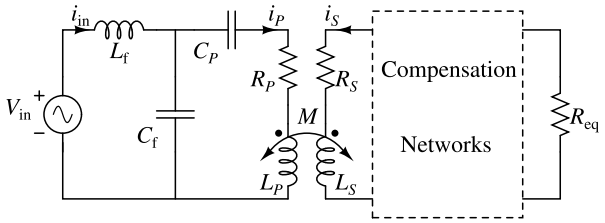

Fig. 2. Equivalent circuit of the WPT system with primary LCC compensation.

To address the drawbacks of the aforementioned EVs detection, this article proposes a method of automatic containment of magnetic field exposure using a novel EV detection method for DWPT systems, which satisfies the following features.

1) Automatic deactivation of the PT to reduce the standby current and the magnetic exposure once the EV departs (from the charging state to the standby state).
2) Automatic activation of full PT once the EV arrives and covers the charger for regular charging (from the standby state to the charging state).
3) Excellent interoperability for various types of receiver-side circuits including different compensation (i.e., s-type, p-type, and LCC-type) and loads.
4) Simple control design instead of clumsy and costly shielding design, extra detection devices, and complex algorithms.
5) No need for wireless feedback communication.

This article is organized as follows. Section II presents the circuit structure used in the proposed DWPT charger and the fundamental theories of the proposed control modulations. In section III, the hybrid control strategy for automatically activating and deactivating system PT is proposed. Section IV analyzes the advantages of interoperability with the proposed strategy. Experimental verifications are given in Section V. Finally, Section VI concludes this article.

II. Analysis of Standby Current Suppression

A. LCC Compensated Transmitter

As shown in Fig. 2, the transmitter circuit of a roadway WPT system typically includes a voltage source, an LCC compensation circuit, and a transmitter coil, while the receiving circuit includes a receiver coil with optional compensation topologies. The LCC compensation network on the transmitter side consists of three components, including an inductor L_f, two capacitors C_f, and C_P. The transmitter coil and receiver coil forms a loosely coupled transformer with L_P, L_S, and M being the primary self-inductance, secondary self-inductance, and mutual inductance respectively. Unless specified, subscripts P and S indicate parameters on the transmitter and receiver sides, respectively. The equivalent

TABLE I
COMPARISONS WITH STATE-OF-THE-ART WORKS

Method and Reference	no extra shielding/sensor	no wireless feedback	simple control	excellent interoperability	component cost	current reduction	field containment
Reactive resonant current loop [15]	×	√	√	not considered	12 switches	×	$< 47.6\%$
nth harmonic shielding coil [16]	×	√	×	√	n HFS coil	×	$< 46.2\%$
Double-reactive shield [18]	×	√	√	not considered	2 coils & 4 capacitors	×	$< 80\%$
TMR sensor detection [22]	×	√	×	not considered	2 TMR sensors	100%	100%
Dual-loop controller method [23]	×	√	×	×	4 coils	100%	100%
Load & mutual inductance estimation [24]	√	×	√	×	voltage & current sensors	$< 83.3\%$	not considered
Parameter estimation method [26]	×	×	√	√	current sensors	100%	not considered
Algorithm based on DC power input [27]	×	×	×	√	4 coils	100%	not considered
Proposed scheme	√	√	√	√	current sensors	$> 90\%$	$> 94.6\%$

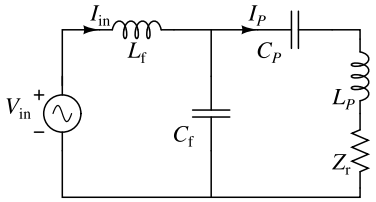

Fig. 3. Primary equivalent circuit.

circuit of the WPT system is shown in Fig. 3. The input voltage is pure sine waveform, and fundamental harmonics approximation is used in this article. Different receivers can be unified as a reflected impedance Z_r on the transmitter side. According to Figs. 2 and 3, R_{eq} is the equivalent load resistance of the passive rectifier and load R_L. The reflected resistance Z_r which is equivalent to the transmitter side is given by

$$Z_r = \frac{(\omega M)^2}{Z_S} \tag{1}$$

where Z_S is the impedance of the receiver-side circuit.

From Fig. 3, the current of the transmitter coil I_P can be obtained from

$$I_P = \frac{V_{in}}{\left(1 - \frac{X_{L_f}}{X_{C_f}}\right)\left(Z_P - jX_{C_f} + Z_r\right) + jX_{C_f}} \tag{2}$$

where Z_P is the impedance of the branch of the transmitter coil, which is given as $Z_P = X_{L_P} - X_{C_P}$. In addition, $X_{L_f} = \omega L_f$, $X_{L_P} = \omega L_P$, $X_{C_f} = (1/\omega C_f)$, and $X_{C_P} = (1/\omega C_P)$ are the inductive reactance of L_f and L_P and the capacitive reactance of C_f and C_P, respectively.

During the standby state, the EV has left already and there is no mutual inductance between the coils. Then, the reflected impedance from the secondary circuit to the primary circuit is equal to zero as well according to (1). Therefore, the standby current can be obtained from (2) as

$$I_{P,\text{standby}} = \frac{V_{in}}{\left(1 - \frac{X_{L_f}}{X_{C_f}}\right)\left(Z_P - jX_{C_f}\right) + jX_{C_f}}. \tag{3}$$

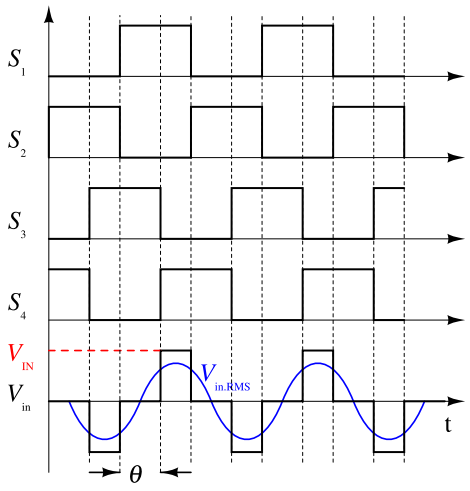

Fig. 4. Typical phase-shifted waveform.

To lower the standby current of the transmitter coil $I_{P,\text{standby}}$ when the receiver is absent, two operations as followed are readily observed in (2).

1) Reduce the input voltage v_{in} through phase-shifted pulse-width modulation (PWM).
2) Modify the circuit impedance by hopping the operating angular frequency ω.

B. Phase-Shifted PWM Control

Phase-shifted PWM has been widely studied and used in the full-bridge inverter to generate a three-level output voltage with variable width. Suppose the full-bridge inverter consists of four switches S_1–S_4, the typical operating waveforms with phase-shifted PWM control are shown in Fig. 4, where V_{IN} is the dc input voltage of the full-bridge inverter and θ is the phase angle. By changing θ, the output voltage of the inverter can be adjusted accordingly, which is given as

$$V_{in.rms} = \frac{2\sqrt{2}}{k\pi} V_{IN} \left|\cos\frac{\theta}{2}\right| \tag{4}$$

where k is the harmonic order and $\theta \in [0°, 180°)$.

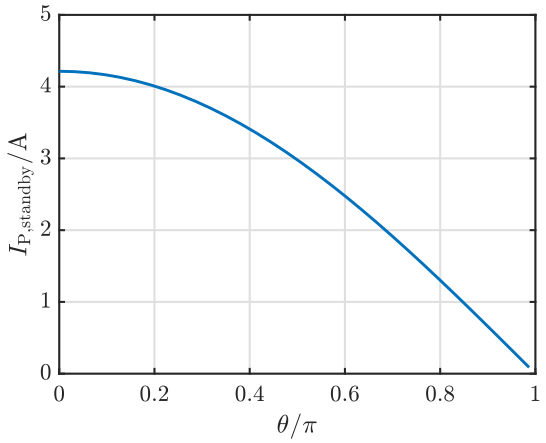

Fig. 5. Standby current $I_{P,standby}$ versus phase-shifted angle θ.

According to (3) and (4), the curve of standby current $I_{P,standby}$ versus phase-shifted angle θ is shown in Fig. 5. It shows that the amplitude of $I_{P,standby}$ decreases monotonously with θ if only the fundamental component is under consideration. Thus, $I_{P,standby}$ can be reduced by applying the phase-shifted angle to the full-bridge inverter.

C. Frequency Hopping

Another way is to hop the operating frequency to an appropriate value. Hence, the derivative of $I_{P,standby}$ is used to investigate the variation in standby current versus frequency. Therefore, it gives

$$\frac{dI_{P,standby}}{d\omega} = \frac{V_{in}\left(3\frac{L_P}{\omega_0^2}\omega^2 - \frac{1}{\omega^2 C_P} - 2L_P\right)}{\left[-\frac{L_P}{\omega_0^2}\omega^3 + 2L_P\omega - \frac{1}{\omega C_P}\right]^2} \tag{5}$$

where ω_0 is the resonant frequency.

Let $(dI_{P,standby}/d\omega) = 0$, the extreme point ω_e is obtained as

$$\omega_e = \frac{\omega_0}{3}\sqrt{1+\sqrt{4-\left(\frac{3L_f}{L_P}\right)}}. \tag{6}$$

Obviously, $\omega_e < \omega_0$ can be easily obtained, which means that the extreme point is to the left of the resonance point.

In addition, according to (5), there are operating points where $I_{P,standby}$ is not differentiable from the frequency. By making the denominator of (5) equal to zero, the points can be derived as

$$\omega_x = \omega_0\sqrt{1\pm\sqrt{\frac{L_f}{L_P}}}. \tag{7}$$

So, there are two undifferentiable points distributed on the left and right sides of the resonance point, respectively, according to (7). And the operating frequency angular has to avoid approaching ω_x. Then, Fig. 6 can be obtained from (6) and (7), which shows the relationship between $I_{P,standby}$ and ω. Then, according to Fig. 6, while the operating frequency ω is higher than the minimum limit threshold point ω_0', $I_{P,standby}$ will reduce. Thus, as long as the target operating frequency

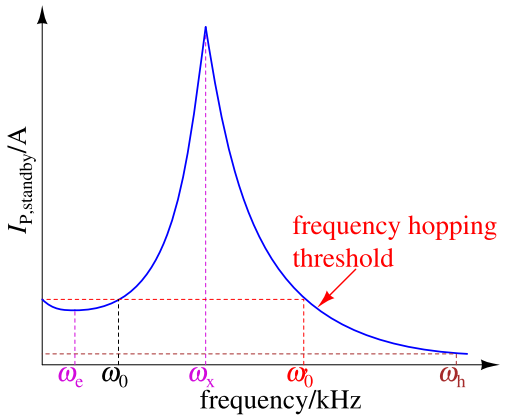

Fig. 6. Relationship between standby current and operating frequency when $\omega \geq \omega_0$.

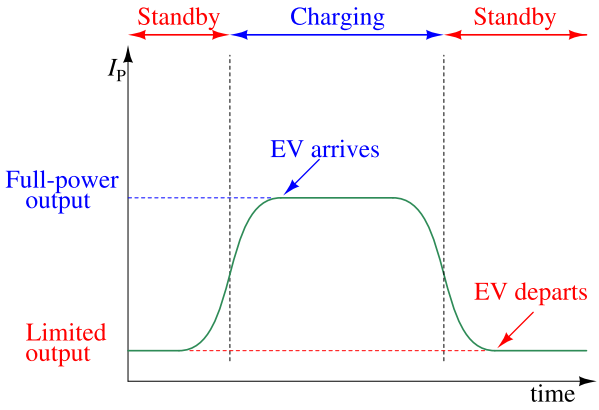

Fig. 7. Objective transmitter coil current variation pattern with EV.

is hopped at ω_h that is far from the threshold ω_0', the standby current can be lowered to the target level.

III. Hybrid Modulation Strategy

Fig. 7 shows the desired state switching process of the DWPT system including the standby state specified with limited power output and the charging state normally with full power output, in which a hybrid modulation strategy with phase-shifted PWM and frequency hopping is designed only for the inverter to extremely limit the output power in the standby state. Moreover, automatic detection is indispensable for the desired state switching process, which can automatically deactivate the chargers while the EV departs and activate them to resume normal charging while EV arrives. In the proposed detection method, with the elimination of extra auxiliary components and wireless feedback communication, only the current factor of the transmitter circuit needed to be adopted.

From Fig. 3, the input current of the LCC compensated network I_{in} can be calculated as

$$I_{in} = \frac{1}{-jX_{C_f}}\left(Z_P - jX_{C_f} + Z_r\right)I_P. \tag{8}$$

Then, a current factor α of the transmitter is defined as

$$\alpha = \frac{|I_{in}|}{|I_P|}. \tag{9}$$

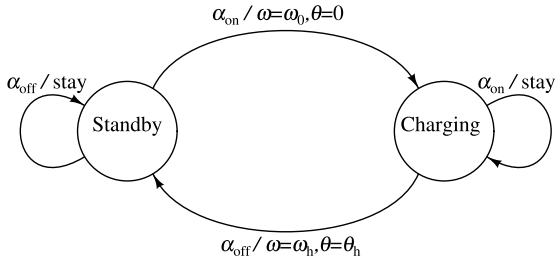

Fig. 8. System state transform diagram.

For automatic EV detection, two major operations for the chargers include deactivation from the charging state to the standby state and activation from the standby state to the charging state as shown in Fig. 8, of which detective conditions are represented as the power-off condition α_{off} and power-on condition α_{on}, respectively. The transition of the dynamic process is divided into loaded condition (EV is departing) and unloaded condition (EV leaves completely).

The system operates at resonance frequency ω_0 during the charging state, and thus (8) can be simplified as

$$I_{\text{in},\omega_0} = \frac{Z_{\text{r}}}{-jX_{C_f}} I_{P,\omega_0}. \tag{10}$$

When EV is departing, the reflected impedance Z_{r} is relevantly changed. Then, as the LCC compensation supplying a constant current I_{P,ω_0} upon the circuit is resonant, I_{in,ω_0} will be sensitively varied according to (10), resulting in the variation in α. After EV leaves the charger completely, it can be realized that α is also equal to zero. Therefore, the variation in α can be used as a detected condition for the system to automatically switch to the standby state, which is summarized as the power-off condition

$$\alpha_{\text{off}} = \begin{cases} \omega_0 C_f Z_{\text{r}}, & \text{loaded condition} \\ 0, & \text{unloaded condition.} \end{cases} \tag{11}$$

Similarly, since the frequency hopping of the hybrid modulation strategy is applied in the standby state, the system operates at ω_{h}. However, the power-on condition α_{on} should be derived by (8) and (9). Thus, whether the EV arrives to couple with the transmitter from standby mode can be detected by the power-on condition

$$\alpha_{\text{on}} = \begin{cases} \frac{1}{-jX_{C_f}}\left(Z_P - jX_{C_f} + Z_{\text{r}}\right), & \text{loaded condition} \\ \frac{1}{-jX_{C_f}}\left(Z_P - jX_{C_f}\right), & \text{unloaded condition.} \end{cases} \tag{12}$$

To more clearly describe the operating process of automatic activation and deactivation, the curves of I_P, I_{in}, and α during the dynamic process are plotted in Fig. 9. In the charging state, the charger normally performs full power output, when the transmitter coil current I_P is constant due to the LCC compensation network. When EV departs, the current I_{in} then drops to zero, which also makes the current ratio α drop below the deactivation threshold α_0. Once the controller judges that α is less than α_{h}, as shown in Fig. 9 at t_0, it will switch to the standby mode and limit the power to reduce the standby current. Then, the ratio α will change to a constant value. During the standby state, although the currents I_{in} and I_P are

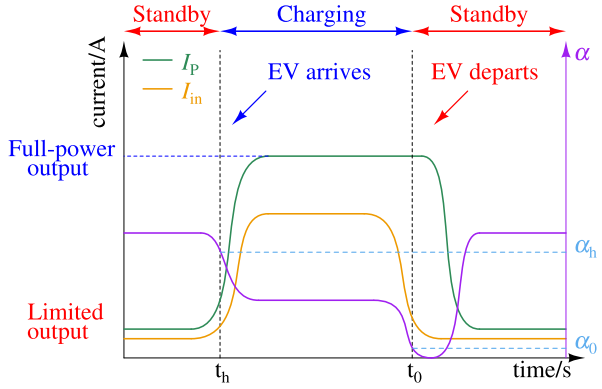

Fig. 9. System state transform diagram.

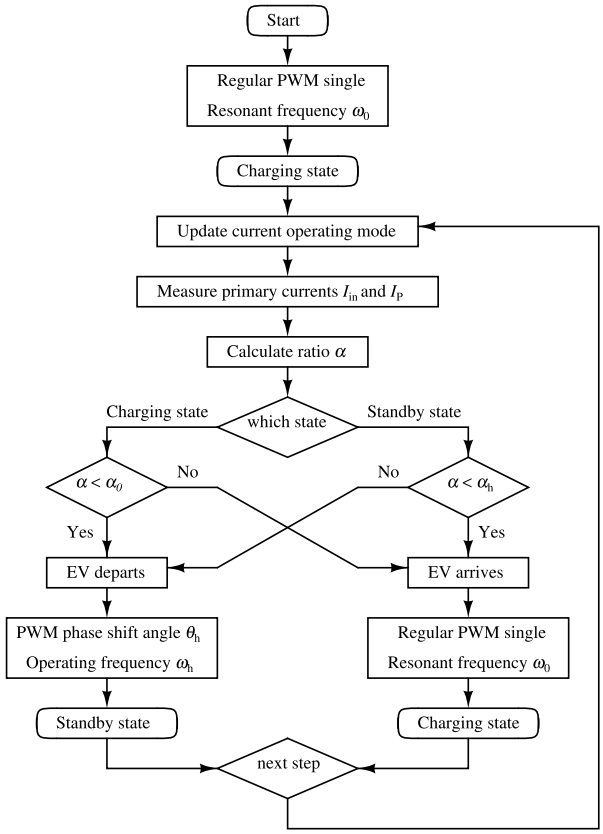

Fig. 10. Flowchart of the proposed control method.

quite small, their amplitudes are still affected by the reflected impedance. Therefore, the current ratio α can still sense the arrival of EV and become below the activation threshold α_{h}, as shown in Fig. 9 at t_{h}. Then, the charger will output the full power and switch to the charging mode.

The flowchart of the whole automatic containment strategy is described in Fig. 10. The controller will calculate α with I_{in} and I_P sampled sequentially and compare it with the corresponding threshold α_0 or α_{h} to determine the next operating state. After that, the controller can relatively regulate the PWM phase angle and hop the operating frequency at the same time. According to the above steps, two operating states can be automatically switched for the system. In addition, α_0 and α_{h} are the detection thresholds selected from (11) and (12)

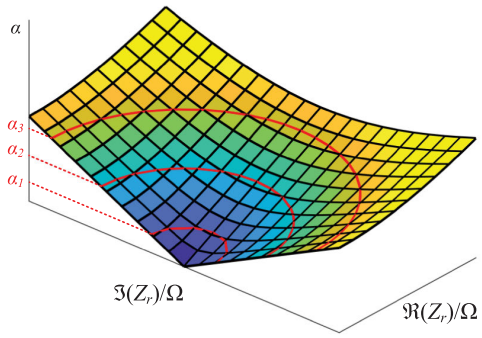

Fig. 11. Variation in current ratio factor α with respect to the reflected impedance $Z_{\rm r}$. The simulation parameters of the LCC DWPT converter are: $L_P = 109\ \mu$H, $C_P = 135.7\ n$F, $L_f = 33.6\ \mu$H, $C_f = 306\ n$F, $R_P = 0.3\ \Omega$, and $R_S = 0.3\ \Omega$. Unless specified otherwise, they will be used in the rest of the article.

for the system to switch operation state, which will be further analyzed in Section IV.

IV. Interoperability of Proposed Method

Typically, the receivers of DWPT systems from different manufacturers are difficult to be unified due to various specifications of batteries, types of compensation topology, and even coupling coefficient k. However, it makes a challenge for the selection of the detection threshold values, α_0 and $\alpha_{\rm h}$. Therefore, interoperability to cope with different receiver compensation networks and load ranges is the key to the feasibility of this method.

A. Interoperability Considerations

Supposed that this method can be implemented to three types of common secondary compensation topologies in practical, s-type, p-type, and LCC-type, within a certain equivalent load range around the optimal value $R_{\rm eq,opt}$ of each compensation, then the interoperability of the method proposed is achieved. However, the desired equivalent load range is selected in the range of $[0.5R_{\rm eq,opt}, 3R_{\rm eq,opt}]$, which is wide enough to match different loads. Besides, the optimal equivalent loads of different compensation topologies are given as

$$R_{\rm eq,opt} = \begin{cases} R_S\sqrt{1+\frac{(\omega_0 M)^2}{R_P R_S}}, & \text{s-type} \\ \omega_0 L_S\sqrt{1+\frac{(L_S)^2 R_P}{(M)^2 R_S}}, & \text{p-type} \\ (\omega_0 L_t)^2\sqrt{\dfrac{R_P}{R_S\left[R_P R_S+(\omega_0 M)^2\right]}}, & \text{LCC-type} \end{cases} \tag{13}$$

where L_t and C_t are the secondary LCC compensation elements, respectively. Meanwhile, the coupling coefficient $k = (M/(L_P L_S)^{1/2})$ is selected in the range of $[0.15, 0.3]$ to simulate the coupling situation of the system in real operation. Therefore, if EVs that meet the above conditions can be detected, the interoperability of this system is considered to be well excellent.

B. Interoperability Analysis Based on Reflected Impedance

The variation in compensation topology, coupling coefficient k, and equivalent load can all be concentrated in the reflected impedance $Z_{\rm r}$ on the primary, which can be expressed as

$$Z_{\rm r} = R + jX \tag{14}$$

where R and X are the real and imaginary parts of $Z_{\rm r}$, respectively.

Hence, based on the distribution range of $Z_{\rm r}$, the conditions required to make the proposed method interoperable can be determined.

From (8) and (14), the equivalent expression for α can be obtained as

$$\alpha = \left|\frac{1}{X_{C_f}}\left(-X_{L_P}+X_{C_P}+X_{C_f}-X+jR\right)\right|. \tag{15}$$

After transformation, it can be observed that R and X are satisfied with

$$R^2+\left[X-\left(-X_{L_P}+X_{C_P}+X_{C_f}\right)\right]^2 = \left(\alpha X_{C_f}\right)^2 \tag{16}$$

where $R \geq 0$.

The variation in current ratio factor α versus the reflected impedance $Z_{\rm r}$ is plotted in 3-D space as shown in Fig. 11. From Fig. 11, a specific α corresponds to a semicircle with a certain radius of αX_{C_f}, which can reliably be used to detect the presence of EV and optionally active or deactivate the circuit.

1) Deactivation Process (Charging State to Standby State): Since the system operates at resonant frequency during the charging state, then Fig. 11 can be simplified as (17) and the corresponding curves of various α ($\alpha = 0.04$, 1.06, and 3.26) graphed in Fig. 12

$$R^2+X^2 = \left(\alpha X_{C_f}\right)^2. \tag{17}$$

Meanwhile, $Z_{\rm r}$ under default conditions including under different compensations, loads, and coupling coefficients at the charging state are also distributed in Fig. 12. As discussed in Section III, the departure of EV results in the convergence of $Z_{\rm r}$ until EV leaves completely where $Z_{\rm r}$ converges to the origin. Thus, a threshold α_0 can be taken between the origin and the region of $Z_{\rm r}$ to detect the departure of EV, which is shown as the bound corresponding to $\alpha = 0.04$ by simulation in Fig. 12. Finally, assuming that the detection accuracy is high enough, there is always a value α_0 that can be found as the deactivation threshold. That is, the deactivation process is interoperable and matches the aforementioned interoperability considerations.

2) Activation Process (Standby State to Charging State): As the system operates at $\omega_{\rm h}$ during standby mode, the center of α becomes somewhere on the imaginary axis of the impedance diagram according to (16). Meantime, $Z_{\rm r}$ under default conditions including under different compensations, loads, and coupling coefficients with operating frequency $\omega_{\rm h}$ are distributed in Fig. 13.

At the standby state, EV is absent, and then the ratio α at this moment is a constant, which is shown as the curve $\alpha_{\rm null}$ in Fig. 13. Moreover, it can be observed that $Z_{\rm r}$ is distributed inside the curve of $\alpha_{\rm null}$, which indicates the presence of EV.

Hence, a threshold $\alpha_{\rm h}$ can be taken between the curve $\alpha_{\rm null}$ and the region of $Z_{\rm r}$ to detect the arrival of EV. Furthermore,

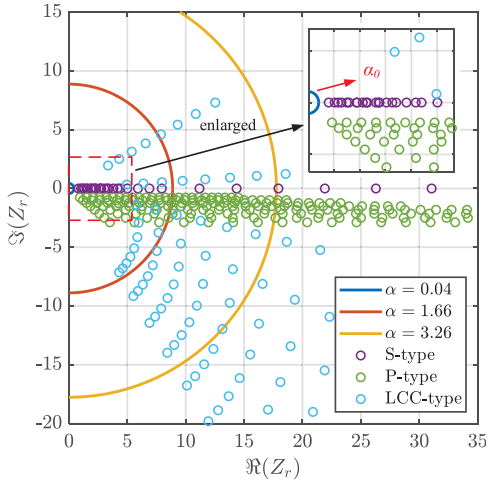

Fig. 12. Distribution of Z_r under different compensations, loads, and coupling coefficients during the deactivation process.

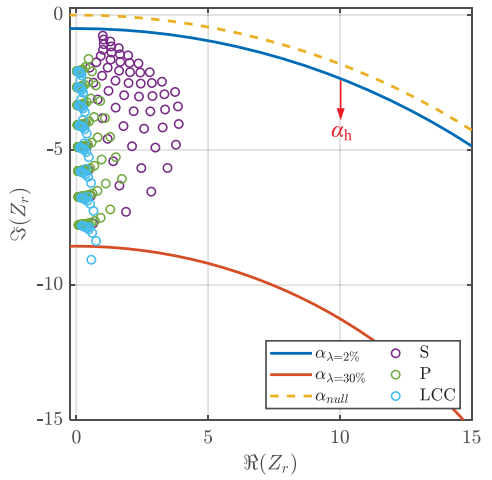

Fig. 13. Distribution of Z_r under different compensations, loads, and coupling coefficients during the activation process.

we define an another factor, λ, that describes the difference between α with respect to the different Z_r and α_{null} at standby state, and its expression is given as

$$\lambda = \frac{\alpha_{null} - \alpha}{\alpha_{null}} \times 100\%. \tag{18}$$

From Fig. 13 and (18), it can be observed that with lower λ, the relevant α is closer to α_{null} when EV arrives but still at standby state. Furthermore, it is feasible to identify Z_r within the target conditions that is closest to α_{null}, with the corresponding current ratio of α_m. Therefore, the threshold α_h can be taken between α_m and α_{null}, such as the simulated bound of $\alpha_{\lambda=2\%}$ in Fig. 13.

With sufficient detection accuracy, a valid activation threshold α_h can always be selected to detect the arrival of EV and activate the system, which indicates that the activation process satisfies the interoperability requirements as well.

C. Selection of the Threshold Current Ratio

With combinations of the deactivation and activation processes, the proposed method is well interoperable as long as

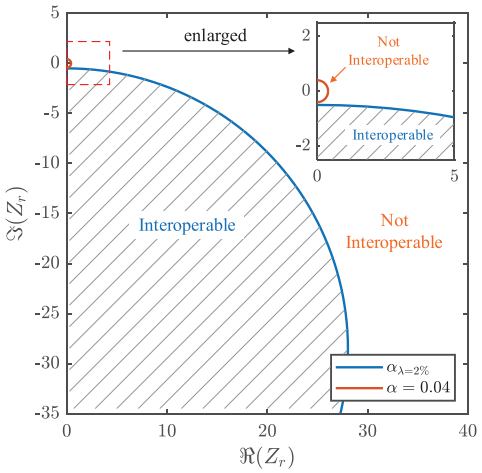

Fig. 14. Interoperable regain of Z_r.

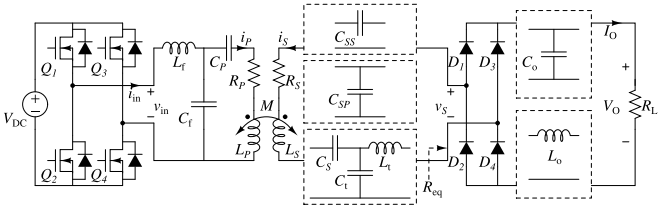

Fig. 15. Schematics of the experiment DWPT converter.

the reflected impedance Z_r of EV load is distributed within the shaded region formed by α_0 and α_h, as shown in Fig. 14, regardless of the secondary compensation and load.

It should be noted that the selection of α_0 and α_h depends on the practical circuit parameters, detection sensitivity, requirement of standby current reduction, and so on. $\alpha_0 = 0.04$ and $\alpha_h = \alpha_{\lambda=2\%}$ are just a set of example values in Fig. 14 for illustration. Nevertheless, the selection of the values of α_0 and α_h will not affect the efficacy of the proposed method.

Meanwhile, to cover as wide a load range as possible, the interoperability analysis considers the range of 0.5–3 times the optimal load corresponding to different compensation circuits, respectively, which covers the width of six times around the optimal load that we think is sufficient to emulate the practical scenarios. However, if the EV load is out of this range, the reflected impedance will change accordingly. α_0 and α_h should be redesigned to ensure the activation and deactivation of the LCC compensated transmitter throughout the whole load range.

To sum up, by selecting the appropriate deactivation thresholds α_0 and activation threshold α_h, the system is always able to detect the departure and arrival of EVs effectively. Thus, the proposed method is considered to be well interoperable.

V. Experimental Verification

A. Specifications and Prototype

The schematics of the proposed LCC IPT converter is shown in Fig. 15. To evaluate the proposed method, an experimental prototype is built, as shown in Fig. 16. The wireless charger system includes the primary dc power supply, full-bridge

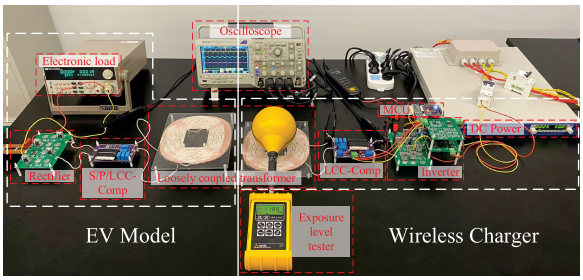

Fig. 16. Prototype of the experiment DWPT converter.

TABLE II
CONVERTER PARAMETERS

Parameters	Symbols	Values
Input voltage	V_{DC}	50V
MOSFETs	Q_1-Q_4	IPP60R165
Diodes	D_1-D_4	MBR20200
Self inductance	L_P, L_S	109 μH, 108.5 μH
Coil resistance	R_P, R_S	0.21 Ω, 0.16 Ω
Output Fliter	C_O, L_o	330 μF, 2 mH
Resonant frequency	f_0	50kHz
Hopping frequency	f_{h}	85kHz
Primary compensation	L_{f}	33.6 μH
	C_{f}, C_P	306 nF, 135.7 nF
Secondary compensation	C_{SS}, C_{SP}	93.7 nF, 93.38 nF
	C_S, C_{t}	124.02 nF, 378.06 nF
	L_{t}	26.8 μH

inverter, LCC compensation network, and transmitter coil. The EV model includes the receiver coil, secondary compensation network, rectifier, and electronic load. The system parameters are given in Table II. An electronic load is used to emulate the EV battery.

B. Measured Standby Current and Magnetic Exposure

To evaluate the ability of the proposed strategy to suppress the standby current and magnetic exposure surrounding the transmitter coil when the EV is absent, an experiment with no modulation applied was performed for comparison.

According to Fig. 17, the original standby current without any modulation is about 6 A as the waveform shown in Fig. 17(a). Compared with the modulated standby current, which is 600 mA as shown in Fig. 17(b), $I_{P,\mathrm{standby}}$ is reduced by about 90%.

Moreover, Fig. 18 shows the magnetic field measured by an exposure level tester above the transmitter in the standby state before and after the proposed modulation. According to the display of the tester shown in Fig. 18(a), the exposure level of the transmitter without modulation is 217.4% of the field strength limit value with reference to the ICNIRP 2010 standard, which means that the exposure greatly exceeds the standard safety limit. Consequently, it may cause injuries to humans and the environment if such systems were implemented at scale. While at the same position, the exposure level with the proposed modulation is merely 11.66% of the standard exposure limit, which is 94.64% less than the original value.

Therefore, the proposed method can significantly suppress the magnetic exposure level generated by the current of the transmitter coil during the standby state, which will enhance the safety and reliability of the system considerably.

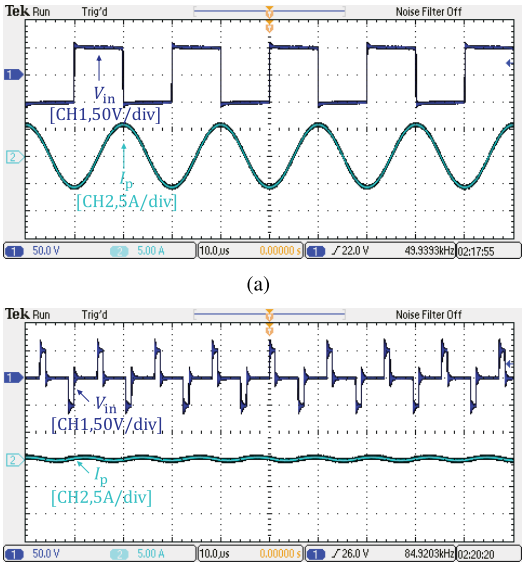

Fig. 17. Measured standby current (a) without modulation and (b) with modulation.

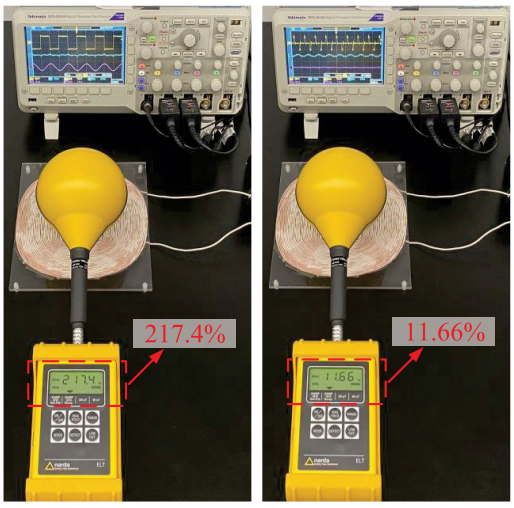

Fig. 18. Measured exposure level during standby state (a) without modulation and (b) with modulation.

C. Measured Operating Process

Fig. 19 shows the operating waveforms when the secondary circuit is compensated with the s-type topology and carries different levels of simulated EV loads. As shown in the enlarged waveform of the charging mode in Fig. 19(a), the system operates initially at the charging mode and the inverter outputs a rectangular wave voltage V_{in} with an amplitude of 50 V from the dc supply. Meantime, the output current I_{o} of 9.2 A represents that the EV is being charged.

Following the proposed operation approach in Section III, once the EV load departs from the transmitter, which can be observed from the waveform of I_{o}, the system is deactivated to the standby state immediately, where the input voltage V_{in}

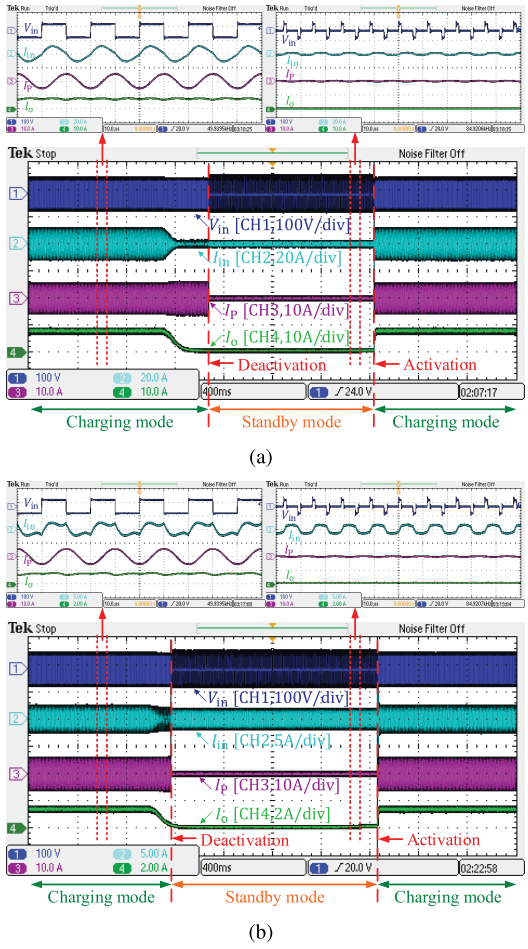

Fig. 19. Measured operating waveforms of the input voltage, the input current, the transmitter coil current, and the output current for the s-type compensated secondary with loads of (a) $R_{\mathrm{L}} = 5.5\ \Omega$ and (b) $R_{\mathrm{L}} = 35\ \Omega$.

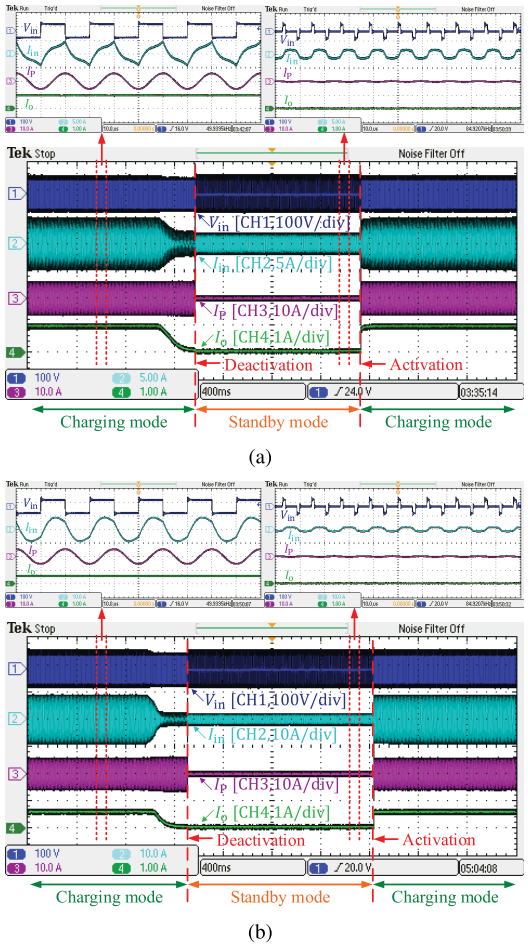

Fig. 20. Measured operating waveforms of the input voltage, the input current, the transmitter coil current, and the output current for the p-type compensated secondary with loads of (a) $R_{\mathrm{L}} = 80\ \Omega$ and (b) $R_{\mathrm{L}} = 500\ \Omega$.

is modulated with a phase-shifted PWM while the operating frequency is hopped to 85 kHz. Moreover, the transmitter coil current I_P is substantially attenuated, which can be observed from the enlarged waveform of the standby mode in Fig. 19(a). Considering the conflict between the hopping frequency f_{h} and the delay time of MOSFETs, a secure phase-shift angle $\theta = 144°$ is selected, leading to a V_{in} of a three-level wave with duty cycle $D = (1/10)$.

In addition, when the EV arrives to couple with the charger during standby state, the system can be successfully activated for full power output in time, which is shown in Fig. 19(a). Afterward, the system will carry on in the charging mode.

D. Interoperability Verification

To verify the interoperability of the system, the three most common types of compensation on the secondary side, s-type, p-type, and LCC-type, are combined with various levels of load for interoperability experiments. According to Section IV-C as long as we select a set of thresholds that can meet the interoperability requirements, we can verify that the strategy is interoperable to different compensations and loads. Therefore, we used the same thresholds in the experiments.

All the loads used in the following experiments are calculated through (13). Fig. 19(a) shows the operating waveforms of the secondary circuit compensated by the s-type network carrying a light load of $R_L = 35\ \Omega$. Combined with the waveform under the heavy load $R_{\mathrm{L}} = 5.5\ \Omega$ shown in Fig. 19(a), it can be seen that the system can reliably switch between both the charging mode and standby mode within a wide enough load range. Since the experimental loads indicate that the applicable load range has covered at least 0.5–3 times the optimal load of LCC-S IPT charger, which can be calculated through (13) with $k = 0.3$, it can be confirmed that the proposed strategy is interoperable for the s-type compensated loads.

Similarly, Fig. 20 shows the operating processes of the system with the p-type compensated secondary under loads of $R_{\mathrm{L}} = 80\ \Omega$ and $R_{\mathrm{L}} = 500\ \Omega$, respectively, which also covers 0.5–3 times the optimal load of the LCC-P IPT system. Besides, LCC-type compensated load is also applicable to the proposed charger as shown in Fig. 21. The experiments verified the operating process under both the loads of $R_{\mathrm{L}} = 3\ \Omega$ and $R_{\mathrm{L}} = 22\ \Omega$, respectively, which covers 0.5–3 times the optimal load for double-sided LCC DWPT systems and fulfills the interoperable requirement as well.

Based on these experiments, it is clear that the proposed strategy has excellent interoperability over a wide enough load range for these typical secondary compensations.

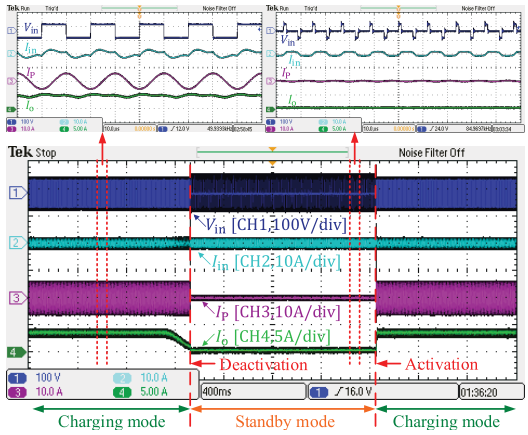

(a)

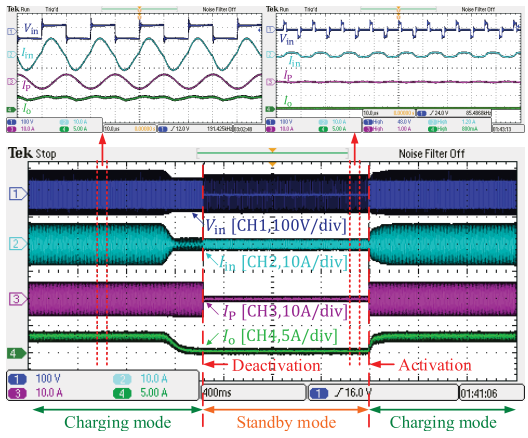

(b)

Fig. 21. Measured operate waveforms of the input voltage, the input current, the transmitter coil current, and the output current for the LCC-type compensated secondary with loads of (a) $R_L = 3\ \Omega$ and (b) $R_L = 22\ \Omega$.

VI. Conclusion

This article proposed a method for automatic containment of magnetic field exposure caused by the standby current in the roadway DWPT system using a novel EV detection method, in which an LCC compensated transmitter with primary-side-only control is applied. The proposed method achieves automatic deactivation and activation without extra detection components and wireless feedback communication. When EV departs, the charger enters the standby state and the standby current of the transmitter coil can be significantly reduced through a hybrid modulation of phase shift PWM control and frequency hopping, which ensures that the surrounding magnetic exposure stays at a safer level. Also, the charger can automatically detect the arrival of EVs and then be activated to charge EVs with full power. Moreover, this method is well interoperable to accommodate various specifications of EV receivers including different types of compensation topologies and a wide range of loads.

References

[1] S. Y. Choi, B. W. Gu, S. Y. Jeong, and C. T. Rim, "Advances in wireless power transfer systems for roadway-powered electric vehicles," *IEEE J. Emerg. Sel. Topics Power Electron.*, vol. 3, no. 1, pp. 18–36, Mar. 2015.

[2] Z. Huang, S.-C. Wong, and C. K. Tse, "Design of a single-stage inductive-power-transfer converter for efficient EV battery charging," *IEEE Trans. Veh. Technol.*, vol. 66, no. 7, pp. 5808–5821, Jul. 2017.

[3] M. Yilmaz and P. T. Krein, "Review of battery charger topologies, charging power levels, and infrastructure for plug-in electric and hybrid vehicles," *IEEE Trans. Power Electron.*, vol. 28, no. 5, pp. 2151–2169, Aug. 2012.

[4] S. Jeong, Y. J. Jang, and D. Kum, "Economic analysis of the dynamic charging electric vehicle," *IEEE Trans. Power Electron.*, vol. 30, no. 11, pp. 6368–6377, Nov. 2015.

[5] Z. Huang, D. Wang, and X. Qu, "A novel IPT converter with current-controlled semi-active rectifier for efficiency enhancement throughout supercapacitor charging process," *IEEE J. Emerg. Sel. Topics Power Electron.*, vol. 10, no. 2, pp. 2201–2209, Apr. 2022.

[6] B. Clerckx, J. Kim, K. W. Choi, and D. I. Kim, "Foundations of wireless information and power transfer: Theory, prototypes, and experiments," *Proc. IEEE*, vol. 110, no. 1, pp. 8–30, Jan. 2022.

[7] J. Huh, S. W. Lee, W. Y. Lee, G. H. Cho, and C. T. Rim, "Narrow-width inductive power transfer system for online electrical vehicles," *IEEE Trans. Power Electron.*, vol. 26, no. 12, pp. 3666–3679, Dec. 2011.

[8] J. Shin et al., "Design and implementation of shaped magnetic-resonance-based wireless power transfer system for roadway-powered moving electric vehicles," *IEEE Trans. Ind. Electron.*, vol. 61, no. 3, pp. 1179–1192, Apr. 2013.

[9] C. C. Mi, G. Buja, S. Y. Choi, and C. T. Rim, "Modern advances in wireless power transfer systems for roadway powered electric vehicles," *IEEE Trans. Ind. Electron.*, vol. 63, no. 10, pp. 6533–6545, Oct. 2016.

[10] A. C. Bagchi, A. Kamineni, R. A. Zane, and R. Carlson, "Review and comparative analysis of topologies and control methods in dynamic wireless charging of electric vehicles," *IEEE J. Emerg. Sel. Topics Power Electron.*, vol. 9, no. 4, pp. 4947–4962, Aug. 2021.

[11] C. Cai, M. Saeedifard, J. Wang, P. Zhang, J. Zhao, and Y. Hong, "A cost-effective segmented dynamic wireless charging system with stable efficiency and output power," *IEEE Trans. Power Electron.*, vol. 37, no. 7, pp. 8682–8700, Jul. 2022.

[12] M. L. Hiles, R. Olsen, K. Holte, D. Jensen, and K. Griffing, "Power frequency magnetic field management using a combination of active and passive shielding technology," *IEEE Trans. Power Del.*, vol. 13, no. 1, pp. 171–179, Jan. 1998.

[13] P. Wu, F. Bai, Q. Xue, X. Liu, and S. Y. R. Hui, "Use of frequency-selective surface for suppressing radio-frequency interference from wireless charging pads," *IEEE Trans. Ind. Electron.*, vol. 61, no. 8, pp. 3969–3977, Aug. 2014.

[14] S. Choi, J. Huh, W. Y. Lee, S. W. Lee, and C. T. Rim, "New cross-segmented power supply rails for roadway-powered electric vehicles," *IEEE Trans. Power Electron.*, vol. 28, no. 12, pp. 5832–5841, Dec. 2013.

[15] J. Kim et al., "Coil design and shielding methods for a magnetic resonant wireless power transfer system," *Proc. IEEE*, vol. 101, no. 6, pp. 1332–1342, Mar. 2013.

[16] B. Sim et al., "A near field analytical model for EMI reduction and efficiency enhancement using an nth harmonic frequency shielding coil in a loosely coupled automotive WPT system," *IEEE Trans. Electromagn. Compat.*, vol. 63, no. 3, pp. 935–946, Dec. 2020.

[17] S. Kim, H.-H. Park, J. Kim, J. Kim, and S. Ahn, "Design and analysis of a resonant reactive shield for a wireless power electric vehicle," *IEEE Trans. Microw. Theory Techn.*, vol. 62, no. 4, pp. 1057–1066, Apr. 2014.

[18] H. Moon, S. Kim, H. H. Park, and S. Ahn, "Design of a resonant reactive shield with double coils and a phase shifter for wireless charging of electric vehicles," *IEEE Trans. Magn.*, vol. 51, no. 3, pp. 1–4, Mar. 2015.

[19] G. R. Nagendra, L. Chen, G. A. Covic, and J. T. Boys, "Detection of EVs on IPT highways," *IEEE Trans. Emerg. Sel. Topics Power Electron.*, vol. 2, no. 3, pp. 584–597, Sep. 2014.

[20] S. A. Al Mahmud, I. Panhwar, and P. Jayathurathnage, "Large-area free-positioning wireless power transfer to movable receivers," *IEEE Trans. Ind. Electron.*, vol. 69, no. 12, pp. 12807–12816, Dec. 2022.

[21] Y. Bu, M. Nishiyama, T. Ueda, Y. Tashima, and T. Mizuno, "Examination of wireless power transfer combined with the utilization of distance detection," *IEEE Trans. Magn.*, vol. 50, no. 11, pp. 1–4, Nov. 2014.

[22] J. T. Vaheeda and B. George, "TMR sensor-based detection of EVs in semi-dynamic traffic for optimal charging," *IEEE Trans. Intell. Transp. Syst.*, vol. 23, no. 8, pp. 1–10, Nov. 2021.

[23] R. Tavakoli and Z. Pantic, "Analysis, design, and demonstration of a 25-kW dynamic wireless charging system for roadway electric vehicles," *IEEE Trans. Emerg. Sel. Topics Power Electron.*, vol. 6, no. 3, pp. 1378–1393, Sep. 2018.

[24] S. Li, L. Wang, Y. Guo, and Z. Liu, "Flexible energy-transfer control of dynamic wireless power transfer system based on estimation of load and mutual inductance," *IEEE Trans. Ind. Appl.*, vol. 58, no. 1, pp. 1157–1167, Jan. 2021.

[25] R. Ruffo, V. Cirimele, M. Diana, M. Khalilian, A. L. Ganga, and P. Guglielmi, "Sensorless control of the charging process of a dynamic inductive power transfer system with an interleaved nine-phase boost converter," *IEEE Trans. Ind. Electron.*, vol. 65, no. 10, pp. 7630–7639, Oct. 2018.

[26] S. Li, C. Liao, and L. Wang, "Online parameter estimation for wireless power transfer systems using the tangent of the reflected impedance angle," *J. Power Electron.*, vol. 18, no. 1, pp. 300–308, 2018.

[27] N. Hasan, H. Wang, T. Saha, and Z. Pantic, "A novel position sensorless power transfer control of lumped coil-based in-motion wireless power transfer systems," in *Proc. IEEE Energy Convers. Congr. Expo. (ECCE)*, Sep. 2015, pp. 586–593.

[28] K. Lee, Z. Pantic, and S. M. Lukic, "Reflexive field containment in dynamic inductive power transfer systems," *IEEE Trans. Power Electron.*, vol. 29, no. 9, pp. 4592–4602, Sep. 2014.

[29] A. Kamineni, M. J. Neath, A. Zaheer, G. A. Covic, and J. T. Boys, "Interoperable EV detection for dynamic wireless charging with existing hardware and free resonance," *IEEE Trans. Transport. Electrific.*, vol. 3, no. 2, pp. 370–379, Jun. 2017.

[30] A. N. Azad, A. Echols, V. A. Kulyukin, R. Zane, and Z. Pantic, "Analysis, optimization, and demonstration of a vehicular detection system intended for dynamic wireless charging applications," *IEEE Trans. Transport. Electrific.*, vol. 5, no. 1, pp. 147–161, Mar. 2018.

Yang Yang was born in Xuzhou, China, in 1998. He received the B.Eng. degree in electrical engineering and automation from the China University of Mining and Technology, Xuzhou, China, in 2020. He is currently pursuing the M.Eng. degree in mechanical engineering with the Shien-Ming Wu School of Intelligent Engineering, South China University of Technology, Guangzhou, China.

His research interests include wireless power transfer and electric vehicles charging.

Jingyu Wang (Student Member, IEEE) was born in Taian, China, in 1996. He received the B.S. degree in electrical engineering and automation from the Hefei University of Technology, Hefei, China, in 2019, and the M.S. degree in electrical engineering from Qingdao University, Qingdao, China, in 2022. He is currently pursuing the Ph.D. degree with the Shien-Ming Wu School of Intelligent Engineering, South China University of Technology, Guangzhou, China.

His current research interest is wireless power transfer.

Zhicong Huang (Member, IEEE) received the B.Eng. degree in electrical engineering and automation and the M.Eng. degree in mechanical and electronic engineering from the Huazhong University of Science and Technology, Wuhan, China, in 2010 and 2013, respectively, and the Ph.D. degree in power electronics from The Hong Kong Polytechnic University, Hong Kong, in 2018.

He is currently an Associate Professor with the Shien-Ming Wu School of Intelligent Engineering, South China University of Technology, Guangzhou, China. From January 2019 to February 2020, he was a Post-Doctoral Fellow under the UM Macao Talent Program, with the State Key Laboratory of Analog and Mixed-Signal VLSI, University of Macau, Macao, China. His research interests include wireless power transfer, power electronics penetrated power system, electric vehicle, and intelligent engineering.

Dr. Huang received the Outstanding Reviewer Award from IEEE TRANSACTION ON POWER ELECTRONICS in 2021.

Io-Wa Iam (Student Member, IEEE) received the B.Sc. degree in electrical and computer engineering from the University of Macau (UM), Macao, China, in 2020, where he is currently pursuing the Ph.D. degree.

His current research interests include power electronics and wireless power transfer.

Dr. Iam was awarded the "Best Track Paper Award" by the IEEE PES Asia-Pacific Power and Energy Engineering Conference in 2019.

Chi-Seng Lam (Senior Member, IEEE) received the Ph.D. degree in electrical and electronics engineering from the University of Macau (UM), Macao, China, in 2012.

He completed the Clare Hall Study Programme with the University of Cambridge, Cambridge, U.K., in 2019. He is currently an Associate Professor with the UM. He has coauthored or co-edited four books and more than 150 technical journals and conference papers. He holds five U.S. and three Chinese patents. His research interests include power quality compensators, renewable energy generation, power management integrated circuits, and wireless power transfer.

Dr. Lam is currently the Chair of the IEEE Macau IES Chapter, the Vice-Chair of the IEEE Macau PES/PELS Joint Chapter and the Secretary of the IEEE IES Technical Committee on Power Electronics. He currently serves as an Associate Editor for the IEEE TRANSACTIONS ON INDUSTRIAL ELECTRONICS, the IEEE OPEN JOURNAL OF THE INDUSTRIAL ELECTRONICS SOCIETY, and the IEEE ACCESS. He was awarded 2021 IEEE ACCESS Outstanding Associate Editor.